




Multiferroic properties of $\text{GdFe}_{0.9}\text{M}_{0.1}\text{O}_3$ ($\text{M} = \text{Ag}^{1+}$, Co^{2+} and Cr^{3+}) nanoparticles and evaluation of their antibacterial activity

Ebtesam E. Ateia^{1,2,a} , B. Hussein¹, Charanjeet Singh³, M. M. Arman¹

¹ Physics Department, Faculty of Science, Cairo University, Giza, Egypt

² Academy of Scientific Research and Technology (ASRT), Cairo, Egypt

³ Department of Electronics, Lovely Professional University, Phagwara, Punjab, India

Received: 16 September 2021 / Accepted: 30 March 2022

© The Author(s) 2022

Abstract Multifunctional nanoparticles NPs with material composition $\text{GdFe}_{0.9}\text{M}_{0.1}\text{O}_3$; $\text{M} = \text{Ag}$, Co , and Cr have successfully been synthesized using the citrate auto-combustion technique. The single phase of the orthorhombic perovskite structure is ratified from the XRD data. The structural, magnetic, and thermoelectric power of the samples along with the results of antibacterial activities are reported in the present manuscript. The variation in the magnetization is argued in view of the strength and type of exchange interaction as well as buckling of the $\langle \text{BO}_6 \rangle$ octahedron. The super exchange interaction between the Fe-O-Fe and the Cr-O-Cr and the randomness of Cr ions in the host lattice site are the main reasons behind the weak ferromagnetism obtained from $\text{GdFe}_{0.9}\text{Cr}_{0.1}\text{O}_3$. Ferroelectricity and antiferromagnetism have a dissimilar origin and appear independently. The origin of antiferromagnetism is the spin canting of the B ions. However, the origin of the ferroelectric properties is the hybridization between B cations and O^{2-} anion. The use of silver metal particles as antibacterial agents is noteworthy due to their advantages in terms of chemical stability, efficacy and long-term durability. These advantages can be extended by considering the relatively low toxicity of these particles to the human body compared to other inorganic metals.

1 Introduction

Recently, orthoferrites become the most interesting materials due to their unique properties [1, 2]. The significant characteristics of orthoferrites are high electrical resistivity, high magnetic nature and low dielectric loss [3, 4]. They can be prepared using facile ways and are modified to a wide variety of levels, even with small structural changes. The functions of these materials can be synchronized by tuning or modifying their magnetic and other physical, as well as chemical, properties [5].

The combination of weak ferromagnetic and antiferromagnetic behavior of orthoferrites nanoparticles NPs gained much attention due to the existence of the multifunctional properties, which make them potential applicants in a variety of applications [6]. Nanomaterials at the nanoscale range enrich the microbial activity owing to their large surface area [7]. The new aspect of nanotechnology is its ability to develop new antibacterial agents through the synthesis of NPs [8]. At a high temperature and pressure, the inorganic antibacterial agents exhibit long self-life and good stability compared to organic antibacterial agents [9]. The sizes of nanomaterials are small enough to easily enter the bacterial cell and restrict its growth [10].

Numerous techniques can be used to synthesize orthoferrite NPs with different morphologies such as solid-state reaction [11], microwave combustion method [12], citrate auto-combustion method [13], sol-gel technique [14], micro-emulsion route [15], and chemical co-precipitation [16].

In particular, citrate auto-combustion technique is quite rapid, simple, high-energy efficiency, good yield, lower cost, cheap starting materials, easy preparation, and low energy consumption.

GdFeO_3 -type distortion plays an important role in the physical properties of the perovskite. The multiferroic perovskite structure GdFeO_3 with element doping has been testified in several investigations [17–22]. Element doping is a significant tool to enhance physical properties. The substitution of A and/or B site atoms in GdFeO_3 can change the Ferro/anti-magnetic and Ferro/anti-electric and affects the relationship between magnetism and ferroelectricity. Partial substitution of cations in the B site has been attempted to modify the antiferromagnetic interaction and turned out to be unsuccessful [23]. The magnitude of the distortion depends on the ionic radii of the cations in the A and B sites. Upon the decrease in ionic radius, the deviation of the Fe-O-Fe bond angle from 180° occurs, i.e., the lattice distortion increases. Besides the bond geometry changes, tilting of the FeO_6 octahedra affects the one-electron bandwidth of the $3d$ electron in a way that it gets smaller with the decrease in ionic radius. The changes from G -type antiferromagnetic, with the magnetic moment in the “ a ” direction to ferromagnetic, with the magnetic moment in the “ c ” direction, occur with increasing GdFeO_3 -type distortion.

^a e-mail: drebtasam2000@yahoo.com (corresponding author)

Ag-doped orthoferrite materials exhibit mixed conduction with a significant amount of Fe^{4+} and a sufficient number of oxygen vacancies leading to mixed ion conduction which can position the material as an attractive cathode material to be used in numerous applications.

In accordance with Goodenough-Kanamori theory, Cr^{3+} is the best choice of substitute element to enhance the magnetization of orthoferrites samples where Fe and Cr ordered at the B site as $\text{Fe}^{3+} (d^5)\text{-O-Cr}^{3+} (d^3)$ would show superior magnetic property due to the super exchange interaction [24, 25]. So, the second choice of transition metal is Cr to induce interesting magnetic and electrical properties.

Substitution of Fe ions with transition ions with different valance gives rise to the coexistence of mobile ions and or vacancy on the B sites. Thus, either the ferromagnetic (FM) or the antiferromagnetic (AFM) interaction can be dominant depending on the B site doping type. Substitution with ions of different ionic radii at a fixed valance modifies the cubic structure in the perovskite-based material and induces lattice distortion in the BO_6 octahedral [26]. The average size of cations in A and B sites has a noticeable effect on the degree of octahedral distortion. This indicates that the size of the cation has a major effect on the bond length B–O, and the bond angle B–O–B, as well as the hopping integral between $\text{Fe}^{3+}/\text{Fe}^{4+}$ degenerate states [27, 28].

In the present study, the effect of identical quantities of numerous valance elements (monovalent, divalent, and trivalent) on the physical properties of the GdFeO_3 is examined. Furthermore, the antibacterial effect of the orthoferrite $\text{GdFe}_{0.9}\text{Me}_{0.1}\text{O}_3$ NPs was screened against Gram-positive bacteria as (*Staphylococcus aureus* and *Bacillus subtilis*) and Gram-negative bacteria as (*Pseudomonas aeruginosa* and *Escherichia coli*) using the inhibition zone method.

2 Experimental work

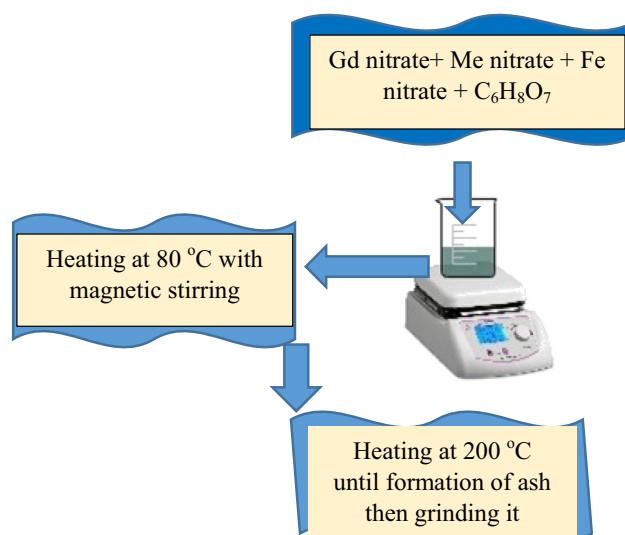
Perovskites $\text{GdFe}_{0.9}\text{Me}_{0.1}\text{O}_3$ ($\text{Me} = \text{Ag}^{1+}, \text{Co}^{2+}, \text{Cr}^{3+}$) were manufactured by using citrate auto-combustion technique. Complete details are published in the previous work and illustrated in Fig. 1 [29].

2.1 Antibacterial activity

The antibacterial activity of $\text{GdFe}_{0.9}\text{Me}_{0.1}\text{O}_3$; $\text{Me} = \text{Ag}, \text{Co}, \text{Cr}$ NPs was evaluated by their zone of inhibitions against six bacterial strains. It was studied using a modified Kirby-Bauer disk diffusion method [30]. Briefly, 100 μl of the test bacteria were grown in 10 ml of fresh media until they reached a count of approximately 108 cells/ml for bacteria [31]. 100 μl of microbial suspension was spread onto agar plates. Isolated colonies of each organism that might be playing a pathogenic role should be selected from primary agar plates and tested for susceptibility by the disk diffusion method.

Plates inoculated with Gram (+) bacteria as *Staphylococcus aureus*, Gram (–) bacteria as *Escherichia coli*, were incubated at 35–37 $^\circ\text{C}$ for 24–48 h. After that, the diameters of the inhibition zones were measured in millimeters [32–35]. Standard disks of Ampicillin (Antibacterial agent) served as positive controls for antimicrobial activity, while filter disks were used as a negative control. Blank paper disks with a diameter of 8.0 mm were impregnated with 10 μl of tested concentration of the stock solutions. When a filter paper disk is placed on agar, the chemical will diffuse from the disk into the agar. The solubility of the chemical and its molecular size will determine the size of the area of chemical infiltration around the disk. If an organism is placed on the agar, it will not grow in the area around the disk. This area of no growth around the disk is known as a “Zone of inhibition” or “Clear zone.”

Fig. 1 Schematic representation for preparation method of $\text{GdFe}_{1.9}\text{Me}_{0.1}\text{O}_3$; $\text{Me} = \text{Ag}, \text{Co},$ and Cr



3 Results and discussion

3.1 Structural analyses

3.1.1 X-ray analysis (XRD)

Figure 2 represents the XRD pattern for the samples of the general formula $GdFe_{0.9}Me_{0.1}O_3$ ($Me = Ag, Co, \text{ and } Cr$). The single phase of the orthorhombic perovskite structure is ratified from the obtained results. This is confirmed by comparing with ICDD cards (01-074-1900). The peak position of $GdFe_{0.9}Me_{0.1}O_3$; $M = Ag, Co, \text{ and } Cr$ are shifted to a higher angle (2θ) compared with the main peak for $GdFeO_3$. This confirms the absence of biphasic structure [36] and the decrease in cell parameters a, c compared to the parent sample.

The crystallite size (L) is detected using the Williamson–Hall relation [37] and the full width at half maximum of the diffraction peak ($\beta_{1/2}$) as mentioned in the previous work [38]. The obtained data are given in Table 1.

The comparison of the lattice parameters (a, b and c), the unit cell volume and the tolerance factor for the investigated samples are given in the table. The data reveal that the Ag substituted sample has the smallest unit cell volume compared to Co, and Cr, in spite of the fact that the Ag^+ has the greatest ionic radii (1.28 Å) [39]. The decrease in the cell volume is due to the increase in Fe^{4+} content, as the size of Fe^{4+} (0.585 Å) is smaller compared to the size of Fe^{3+} (0.645 Å). The valence exchange between Fe^{4+}/Fe^{3+} leads to the formation of oxygen vacancy that has an effect on the unit cell volume. This behavior agrees well with the obtained data for Ca doping $PbTiO_3$ [40].

The specific surface area (S) of the grain is calculated using the following equation [41] and the obtained data are given in the table.

$$S = \frac{\text{grain surface area}}{\text{grain mass}} = \frac{6000}{LD_x} \tag{1}$$

Additionally, the theoretical density (D_x) is calculated from the following equation [42]:

$$D_x = \frac{ZM}{N_A V} \tag{2}$$

where Z is the number of molecules per unit cell, M is the molecular weight, N_A is the Avogadro’s number and V is the volume of the unit cell, and the obtained data are given in the table.

Fig. 2 The XRD pattern for $GdFe_{0.9}Me_{0.1}O_3$ ($M = 0.0, Ag, Co \text{ and } Cr$) nanoparticles

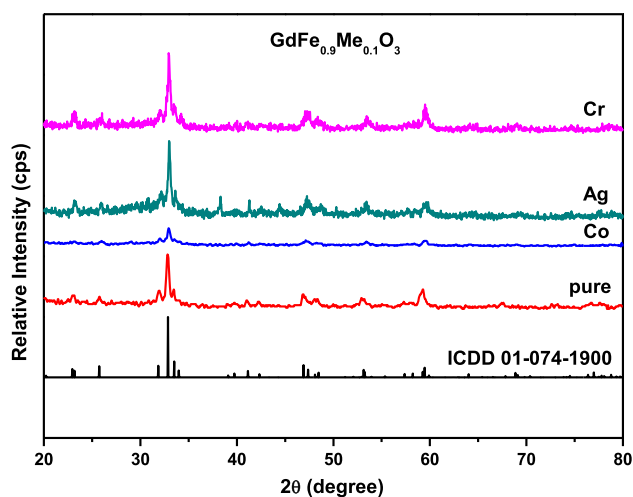
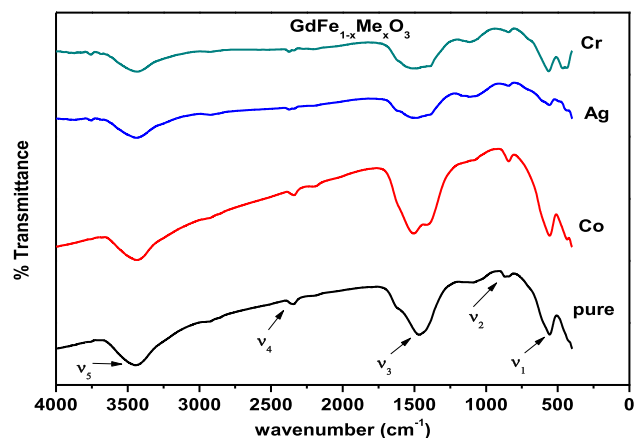


Table 1 Lattice parameters, volume of the unit cell (V), theoretical density (D_x), crystallite size (L), the tolerance factor (T), dislocation density (δ) and specific surface area (S) for the investigated samples

Samples	a (Å)	b (Å)	c (Å)	V (Å ³)	D_x (g/cm ³)	L (nm)	c/a	T	$\delta \times 10^{-3}$	$S \times 10^7$
GdFeO ₃	5.577	7.679	5.372	230.09	7.536	16.5	0.963	0.871	3.67	4.83
GdFe _{0.9} Co _{0.1} O ₃	5.569	7.689	5.319	227.83	7.620	12.1	0.955	0.872	6.83	6.51
GdFe _{0.9} Cr _{0.1} O ₃	5.522	7.683	5.350	229.95	7.629	26.7	0.969	0.875	1.40	2.95
GdFe _{0.9} Ag _{0.1} O ₃	5.522	7.684	5.349	226.93	7.793	24.4	0.969	0.849	1.68	3.16

Fig. 3 FTIR spectrum for $\text{GdFe}_{0.9}\text{Me}_{0.1}\text{O}_3$ (Me = 0.00, Ag, Co and Cr) multiferroics



It is revealed that the addition of B cations (Co^{2+} , Ag^{1+} , and Cr^{3+}) with different valences increases D_x compared to the parent sample. This increase can be attributed to that the ionic radii of Co (0.745 Å), and Ag (1.28 Å) are higher than the ionic radius of Fe^{3+} (0.645 Å) ion. On the other side, Cr substitution induces a higher oxidation state [43, 44]. This may induce defects that affect the magnetic properties of the prepared sample as will be discussed later [45].

As shown from table, $\text{GdFe}_{0.9}\text{Ag}_{0.1}\text{O}_3$ -doped sample has the largest density compared to $\text{GdFe}_{0.9}\text{Co}_{0.1}\text{O}_3$ and $\text{GdFe}_{0.9}\text{Cr}_{0.1}\text{O}_3$ substituted samples. This is due to the high atomic weight (103.5) and high density (10.49 g/cm^3) of Ag compared to Cr and Co-doped samples. In fact, the increment rate of the molecular mass is more than that of the lattice parameter.

The dislocation density (δ) [46, 47] has also been determined using the following equation:

$$\delta = \frac{1}{L^2} \quad (3)$$

The tolerance factor (T) is a geometrical factor characterizing the size mismatch which takes place when a site cation is very small that is accommodated into the BO_6 octahedra of the three-dimensional networks. As the “ T ” decreases, the bond angle (θ) decreases, and orthorhombic cell distortion increases. For $\text{GdFe}_{0.9}\text{Ag}_{0.1}\text{O}_3$, there is an increase in the orthorhombic distortion as a result of doping Ag at the expense of Fe because of the mismatch between the ionic radii of Ag^+ and Fe^{3+} (1.28 Å and 0.645 Å, respectively). The variation in the ionic radii leads to a change in the “ T ,” as well as in the bond angle $\theta_{\text{Fe-O-Fe}}$. This is a measure of the tilting of the octahedral and is also directly linked to orthorhombic cell distortion [48].

On the other hand, when adding Cr by 10% at the expense of Fe in $\text{GdFe}_{0.9}\text{Cr}_{0.1}\text{O}_3$, an increase in the “ T ” compared with the parent sample is observed. The reduced distortion can be attributed to the variance in the ionic radii between Cr (0.615 Å) and Fe (0.645 Å) considering the oxidation state 3+ and octahedral coordination for both atoms [49].

3.1.2 Fourier transform infrared spectroscopy (FTIR)

FTIR spectra of Multiferroic samples $\text{GdFe}_{0.9}\text{Me}_{0.1}\text{O}_3$ ($M = \text{Ag, Co, and Cr}$) are displayed in Fig. 3. The detected bands in the range from ~ 420 to 435 cm^{-1} are recognized Fe–O or Co–O bending vibrations of FeO_6 . These bands are sensitive to Fe–O–Fe bond angle [50]. In the present case, this band does not seem due to the technical limitations of the device. The presence of antisymmetric stretching vibrations Fe–O or Co–O bonds in octahedral is ratified via the presence of ν_1 mode around 556 cm^{-1} . The two observed bands are the most significant issues in the perovskite oxides [51]. The ν_3 mode is detected around 1446 cm^{-1} , which corresponds to symmetric carboxylate stretches (COO^-), while C–H bend mode (ν_2) appears at 850 cm^{-1} . The symmetric stretching vibrational band of carboxyl root is represented by a small band (ν_4) at about 2345 cm^{-1} [52]. Additionally, ν_5 mode represents the symmetric and asymmetric stretching vibration of water molecules and is detected at 3445 cm^{-1} [53]. The other detected bands with a small intensity appear around 2400 cm^{-1} which is due to O–H (carboxylic acids) [54].

The observed peaks are the main features in the perovskite oxides [55] regardless of the doping of transition metals either Ag, Co, or Cr which does not result in any significant shift of the IR data.

It has been observed that the broadness of the bands is greater for $\text{GdFe}_{0.9}\text{Ag}_{0.1}\text{O}_3$. This change may be due to a change in the tolerance factor value which decreases the distortion of the structure.

3.1.3 High-resolution transmission electron microscope (HRTEM)

High-resolution transmission electron microscopy (HRTEM) is utilized to scrutinize the morphology and crystalline structure of the investigated NPs. Figure 4a–c displays the HRTEM images of the investigated samples. The agglomeration of the nanoparticles with uniform size and orthorhombic shape is observed. This reveals that the prepared samples exhibit fine nano-structure of the orthoferrites.

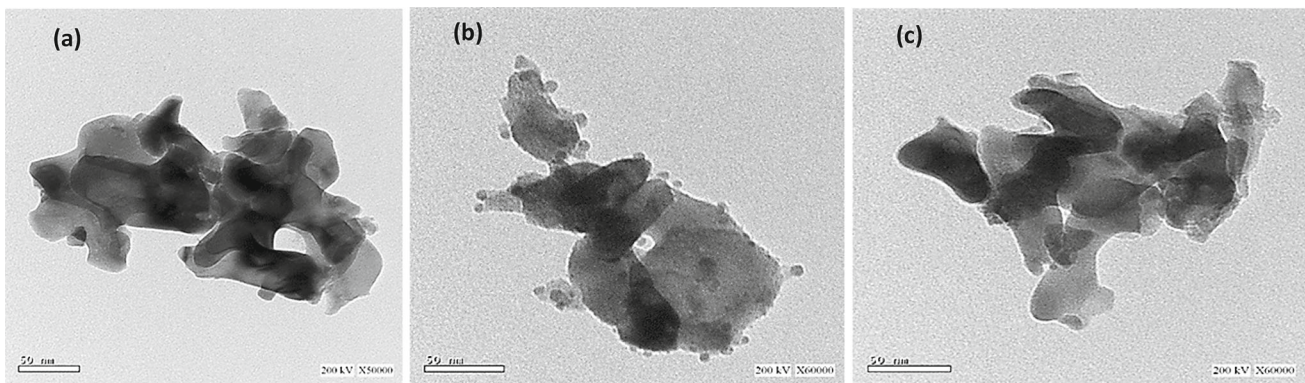


Fig. 4 a–c HRTEM images for $\text{GdFe}_{0.9}\text{Me}_{0.1}\text{O}_3$ multiferrites, **a** Co, **b** Ag **c** Cr

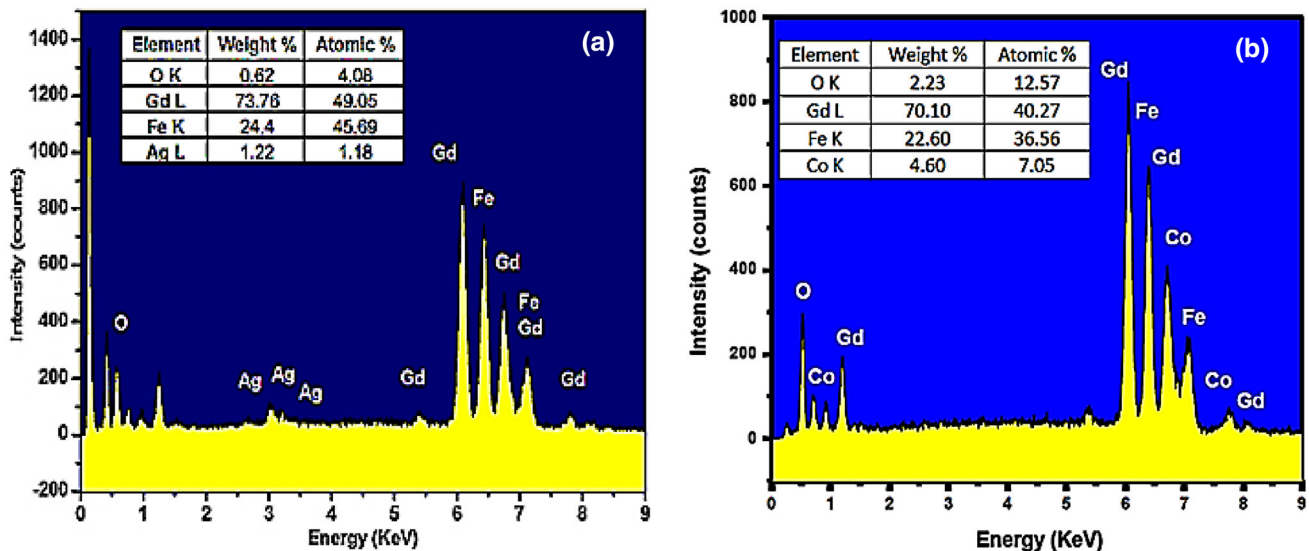


Fig. 5 a, b The energy-dispersive X-ray analysis for **a** $\text{GdFe}_{0.9}\text{Ag}_{0.1}\text{O}_3$ and **b** $\text{GdFe}_{0.9}\text{Co}_{0.1}\text{O}_3$ multiferrite samples

3.1.4 Energy-dispersive X-ray analysis (EDAX)

The energy-dispersive X-ray analysis (EDAX) of $\text{GdFe}_{0.9}\text{Me}_{0.1}\text{O}_3$; (Me = Co, and Ag) is shown in Fig. 5a, b. The relative elemental concentrations of Gd, Fe, Co, Ag, and O in $\text{GdFe}_{1-x}\text{M}_x\text{O}_3$ are determined with the help of EDAX spectra. The EDAX spectra clearly reveal that the samples are without any impurity and also the relative concentrations of Gd, Co, Ag, and Fe are close to the expected concentration.

3.2 Magnetic properties

The magnetization hysteresis loops of the orthoferrites samples are shown in Fig. 6a, b. Generally, the substitution in the B site by monovalent and divalent is expected to convert a fraction of Fe^{3+} to Fe^{4+} . Though, Fe^{4+} is difficult to form at ambient pressure. Therefore, the imbalance of charge introduced by Ag^{1+} , and Co^{2+} cations have to be compensated by oxygen deficiency [56]. The systematic change in the saturation magnetization with different ionic radii/valence of the cation possibly indicates that the oxygen deficiency alone may not cause the enhanced magnetization. It may be related to the progressive suppression of spiral spin structure and/or increase in the canting angle of antiferromagnetically coupled layers due to tilting of $\text{FeO}_{6.8}$ octahedra. Thus, it is observed that the magnetization is unsaturated even at a very high field and the coercivity of all samples is found to be quite low, i.e., in the range of 100–700 Oe.

The weak ferromagnetism is detected for $\text{GdFe}_{0.9}\text{Cr}_{0.1}\text{O}_3$ NPs. This behavior is due to different issues. The uncompensated canted spins from the surface, as well as the internal canted spin, are the main issue. The second issue is the interaction of Cr–O–Cr and the Cr^{3+} (d^3) dilutes the AFM (Fe–O–Fe (d^5)) matrix leading to reduced magnetization as discussed by Copogna et al. [57]. The third is due to the cluster or impurity phase coexisting in samples [58].

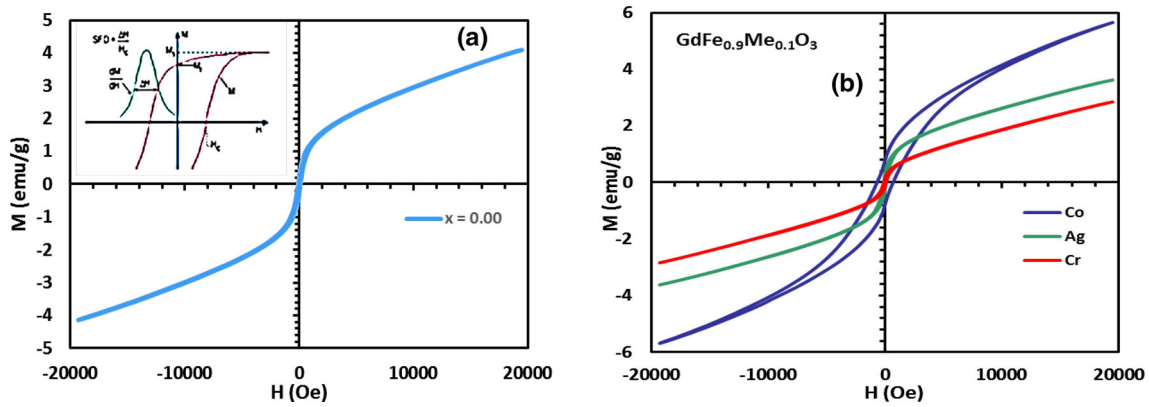


Fig. 6 a, b The magnetization hysteresis loops of the investigated samples a pure sample and b substituted samples

Table 2 Shows the remnant magnetization (M_r), saturation magnetization (M_s), squareness (M_r/M_s) and coercivity (H_c), energy loss, ionic radii of the investigated samples

Samples	M_r (emu/g)	M_s (emu/g)	M_r/M_s	H_c (Oe)	Energy loss (erg/g)	Ionic radii (Å)
GdFeO ₃	0.292	4.119	0.071	106	1432	0.645
GdFe _{0.9} Co _{0.1} O ₃	0.796	5.672	0.140	702	13,242	0.745
GdFe _{0.9} Ag _{0.1} O ₃	0.252	3.621	0.069	93	925	1.28
GdFe _{0.9} Cr _{0.1} O ₃	0.126	2.844	0.044	89	904	0.615

Table 2 shows the remnant magnetization (M_r), saturation magnetization (M_s), and coercivity (H_c), squareness for the investigated samples. It is clear that the decrease in H_c for Cr can be attributed to the dilution of long-range Fe–O–Fe interaction, which indicates that Cr acts as an antiferromagnetic ion in the investigated samples. A similar signature has been detected for Cr-substituted LaFeO₃.

The “ M_s ” values for GdFe_{0.9}Cr_{0.1}O₃ and GdFe_{0.9}Ag_{0.1}O₃ decrease compared to the pure samples as given in the table. This decrease is due to diluting the magnetization in the B site by increasing accommodation of the less magnetic moment Cr³⁺ (3.87 μ_B), and Ag¹⁺ (3 μ_B) instead of Fe³⁺ (5 μ_B) ions. Moreover, this causes the weakening of the direct exchange magnetic interaction between the crystal sublattices [59–61].

As shown from the table, the squareness values are less than 0.5 which suggests that the particles are not in a predominant single domain state despite their small size. When $R < 0.5$, the particles interact by magnetostatic interaction according to Z.L. Wang [62, 63]. In the present case, the calculated values assure that a magnetostatic interaction is possible with an expected spin coupling between the layers of the nanoparticles.

3.3 Electrical properties

3.3.1 Ferroelectric properties

The origin of the ferroelectric properties is the covalent bond between the B cations and O anion. The B ions shift from the center of <BO₆> octahedra toward the three oxygens to form a strong covalent bond. Figure 7a–d illustrates the room temperature P–E hysteresis loops of GdFe_{0.9}Me_{0.1}O₃ (Me = Ag, Co, Cr).

All samples exhibit clear hysteric behavior indicating ferroelectric nature. It is observed that the P–E loops are unsaturated. This can be attributed to the pinning of the domain walls due to the presence of the oxygen vacancies. The values of the ferroelectric parameters like remnant polarization (P_r), saturation polarization (P_s), and coercive electric field (E_c) are given in Table 3.

At ambient temperature, and increasing electric field, the P_s , P_r are found to be maximum for GdFe_{0.9}Co_{0.1}O₃. The detected increase in P_r polarization for GdFe_{0.9}Co_{0.1}O₃ may be due to both, reduction in leakage current and the small crystallite size [64]. As shown from the figure, the loops are slightly shifted around the origin. This abnormality can be clarified by the existence of an internal electric field originating from the off-centering and intrinsic movement of bound electrons inside the samples. The increase in the coercive field for GdFe_{0.9}Co_{0.1}O₃ can be attributed to dipole friction that arises owing to the domain orientation [65].

Finally, one can conclude that the investigated samples have antiferromagnetic and ferroelectric behaviors simultaneously. The origin of antiferromagnetism is the spin canting of the B ions, while the origin of the ferroelectric properties is the hybridization between B cations and O²⁻ anion. Ferroelectricity and ferromagnetism have a dissimilar origin and appear independently of one another.

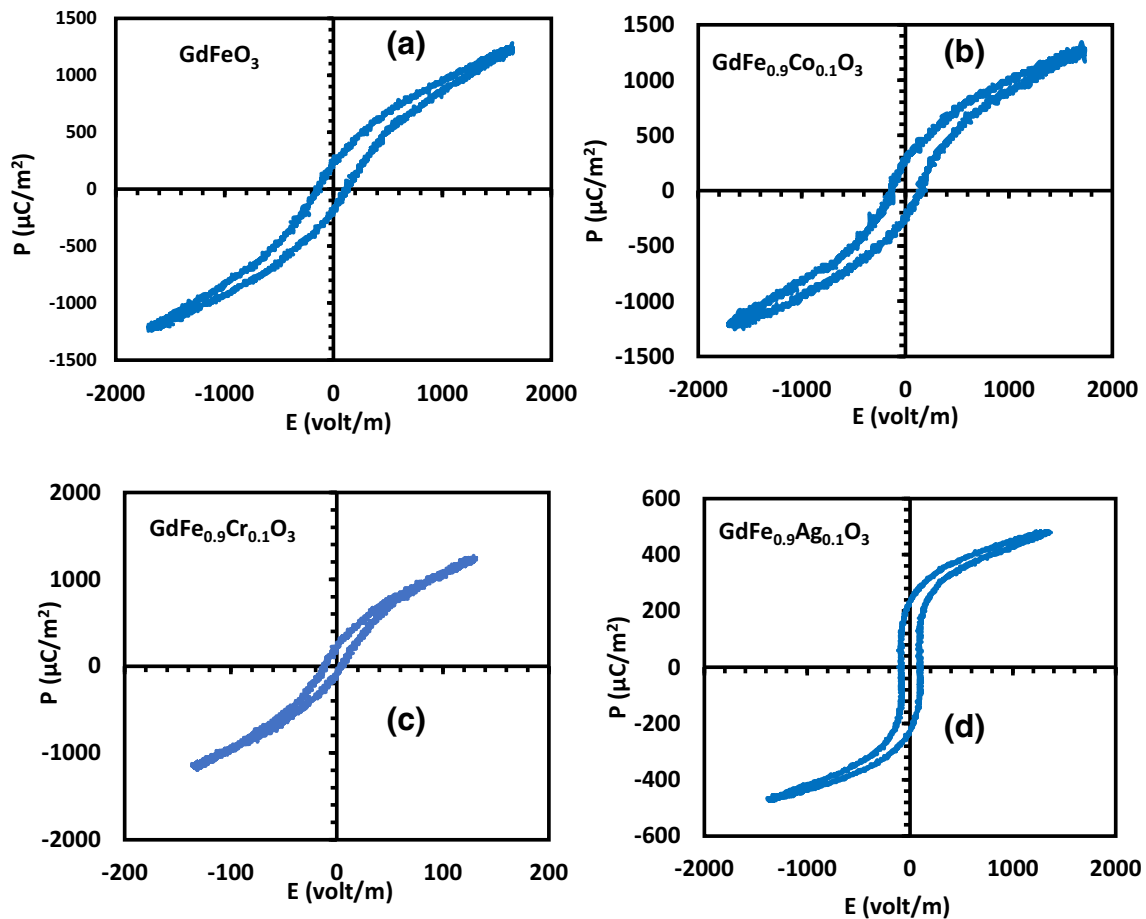


Fig. 7 a–d Illustrates the room temperature P–E hysteresis loops of **a** GdFeO₃, **b** GdFe_{0.9}Co_{0.1}O₃, **c** GdFe_{0.9}Cr_{0.1}O₃ and **d** GdFe_{0.9}Ag_{0.1}O₃

Table 3 The saturation polarization (P_s), remanent polarization (P_r), and coercive electric field (E_c) for GdFe_{0.9}Me_{0.1}O₃ (M = Ag, Co, and Cr)

Transition metal	P_s ($\mu\text{C}/\text{m}^2$)	P_r ($\mu\text{C}/\text{m}^2$)	E_c (V/m)
GdFeO ₃	1227	229	142
GdFe _{0.9} Ag _{0.1} O ₃	479	224	117
GdFe _{0.9} Co _{0.1} O ₃	1255	263	174
GdFe _{0.9} Cr _{0.1} O ₃	1224	119	5

3.3.2 Thermoelectric power

The valence of the cations, the spin of the charge carriers, the symmetry of the structure, and the strengths of the crystal field are the main issues that affect the thermoelectric power of samples. Figure 8a–d shows the temperature dependence of the Seebeck coefficient (dV/dT) of the GdFe_{0.9}Me_{0.1}O₃ (Me = Co, Cr and Ag) nanoparticles. In the present case, the value of the (dV/dT) changes from $-Ve$ to $+Ve$ depending on the types of dopants. The majority carriers of the GdFeO₃ ($x = 0$) are electrons over the temperature range of 300–600 K. Figure 8b shows the increase in the Seebeck coefficient with increasing temperature up to $T_C = 453$ K. This observation can be attributed to the formation of Co³⁺ high spin state configuration ($t_{2g}^4 e_g^2$) at high temperature [66]. The spin entropy is most probably the reason for the large thermopower found in GdFe_{0.9}Co_{0.1}O₃ sample.

According to Mizusaki et al. [67], the sign change can be attributed to the concentration of cation defects. This means that the deviation from the stoichiometric cation composition causes an important discrepancy in the Seebeck coefficient.

3.4 Antibacterial activities of GdFe_{0.9}Me_{0.1}O₃

Figure 9a, b shows the variation in the zone of inhibition caused by the prepared GdFe_{0.9}Cr_{0.1}O₃ and GdFe_{0.9}Ag_{0.1}O₃ samples. The nanoparticle sizes of the prepared samples are one of the chief parameters for the enhancement of efficiency for the activity of antibacterial. The magnetic NPs are accepted as the one of attractive carrier systems due to their physicochemical properties such

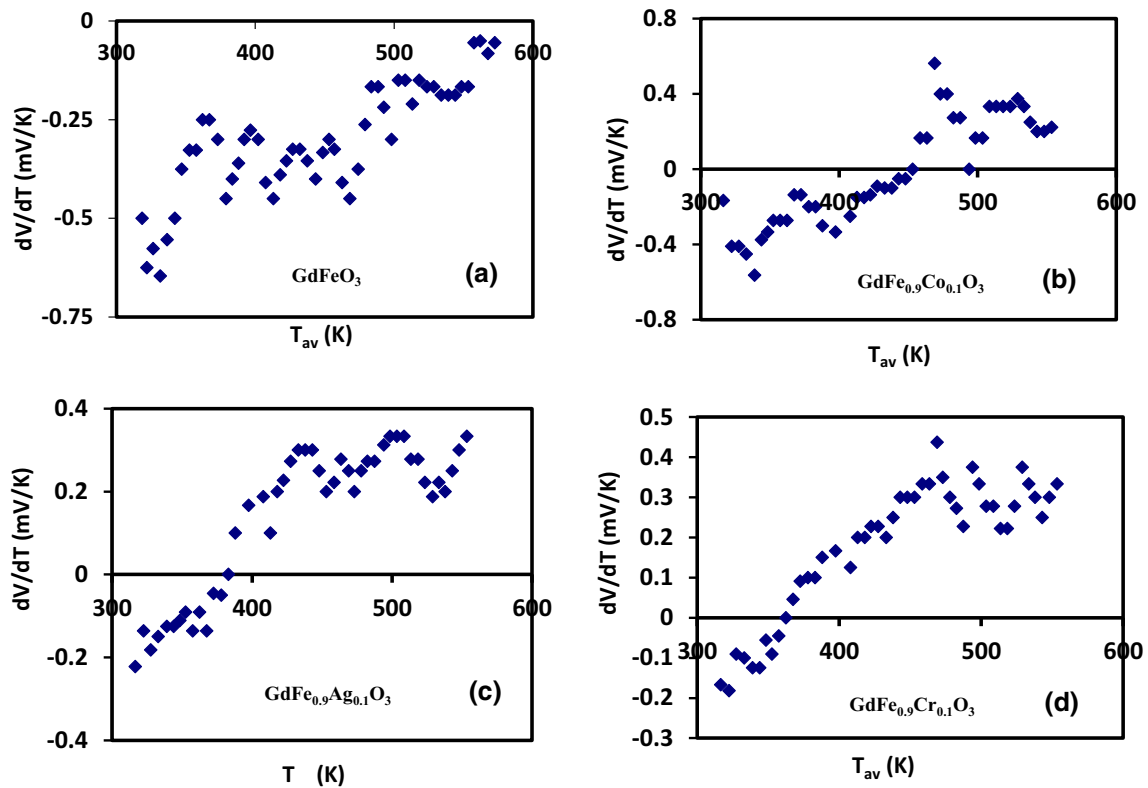


Fig. 8 a–d The temperature dependence of Seebeck coefficient of the **a** GdFeO_3 , **b** $\text{GdFe}_{0.9}\text{Co}_{0.1}\text{O}_3$, **c** $\text{GdFe}_{0.9}\text{Ag}_{0.1}\text{O}_3$, and **d** $\text{GdFe}_{0.9}\text{Cr}_{0.1}\text{O}_3$

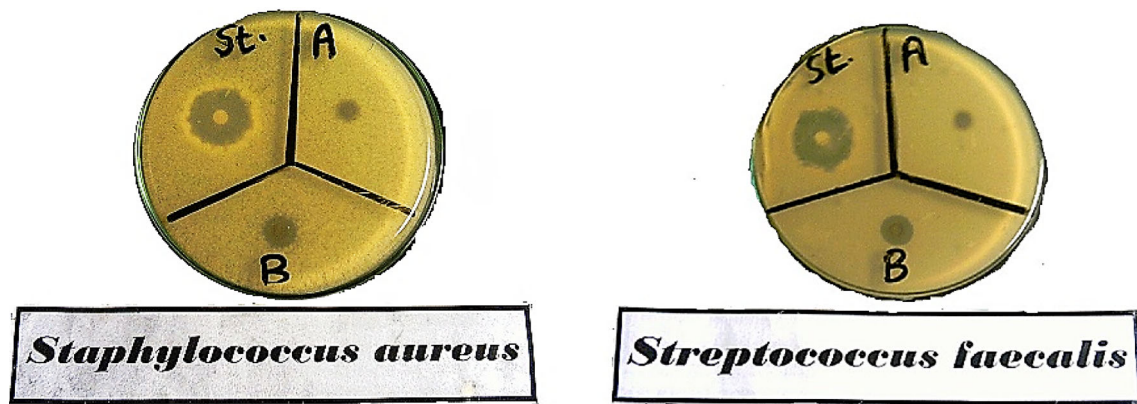


Fig. 9 a, b The variation in the zone of inhibition of $\text{GdFe}_{0.9}\text{Cr}_{0.1}\text{O}_3$ and $\text{GdFe}_{0.9}\text{Ag}_{0.1}\text{O}_3$ samples for different antibacterial **a** staphylococcus aureus and **b** streptococcus faecalis

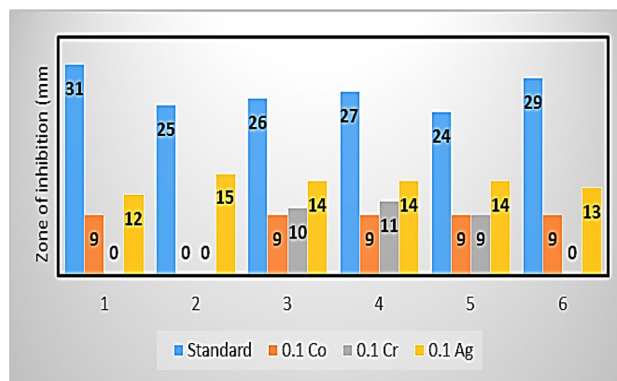
as good stability, biocompatibility, colloidal stability, effective treatment at lower doses, and controllable sizes [68]. However, the probable mechanisms of antimicrobial activity for the NPs can be attributed to numerous issues. The first one is interference through cell wall synthesis. The second and third are suppression through protein biosynthesis and the disturbance of primary metabolic pathways, respectively [69, 70].

Generally, the activity of antibacterial of the samples is mainly related to the existence of holes/electrons generated by electrovalence compensation in the samples. Furthermore, the antibacterial effect principally depends on the NPs size and their distribution [71]. Smaller nanoparticles, due to having a much larger surface area, can greatly increase the production of the reactive oxygen species which is a significant parameter essential for antibacterial applications. The average amount of inhibition zone with its standard deviation is determined in Table 4. However, the $\text{GdFe}_{0.9}\text{Co}_{0.1}\text{O}_3$, $\text{GdFe}_{0.9}\text{Cr}_{0.1}\text{O}_3$ have weak antibacterial activity as shown in the Table and Fig. 10. These samples cannot be able to destroy the bacterial species.

The obtained data revealed that the $\text{GdFe}_{0.9}\text{Ag}_{0.1}\text{O}_3$ NPs are relatively effective than other investigated samples. This is due to the fact that the antimicrobial activity of $\text{GdFe}_{0.9}\text{Ag}_{0.1}\text{O}_3$ depends on the amount of monovalent ions released and interacts with

Table 4 The antibacterial activity for $\text{GdFe}_{0.9}\text{Co}_{0.1}\text{O}_3$, $\text{GdFe}_{0.9}\text{Cr}_{0.1}\text{O}_3$ and $\text{GdFe}_{0.9}\text{Ag}_{0.1}\text{O}_3$ samples

Types of antibacterial	Standard	Co	Cr	Ag
<i>Bacillus Subtilis</i>	31	9	0	12
<i>Staphylococcus Aureas</i>	25	0	0	15
<i>Straptococcus Faecalis</i>	26	9	10	14
<i>Escherichia Coli</i>	27	9	11	14
<i>Neisseria Gonorrhoeae</i>	24	9	9	14
<i>Pseudomonas Aeruginosa</i>	29	9	0	13

Fig. 10 The antibacterial activity for $\text{GdFe}_{0.9}\text{Co}_{0.1}\text{O}_3$, $\text{GdFe}_{0.9}\text{Cr}_{0.1}\text{O}_3$ and $\text{GdFe}_{0.9}\text{Ag}_{0.1}\text{O}_3$ samples

thiol groups existing in bacterial enzymes. This destroys the bacterial species [72]. The use of silver metal particles as antibacterial agents is noteworthy due to their advantages in terms of chemical stability, resistance to temperature variations, efficacy, and long-term durability. These advantages can be extended by considering the relatively low toxicity of these particles to the human body compared to other inorganic metals [44].

4 Conclusion

The perovskite samples were synthesized by the citrate auto-combustion technique. The single phase of the orthorhombic perovskite structure is ratified from the X-ray data.

The variation in the magnetization by Co^{2+} , Cr^{3+} , and Ag^{1+} ion substitution depends on the strength and type of exchange interaction and/or canting angle, as well as buckling of the $\langle \text{BO}_6 \rangle$ octahedron.

The deviation from the stoichiometric cation composition causes a significant variation in the Seebeck coefficient.

The obtained data revealed that the $\text{GdFe}_{0.9}\text{Ag}_{0.1}\text{O}_3$ nanoparticles exhibited enhanced antibacterial activity compared to $\text{GdFe}_{0.9}\text{Co}_{0.1}\text{O}_3$ and $\text{GdFe}_{0.9}\text{Cr}_{0.1}\text{O}_3$ samples.

The Ag ions accompanying GdFeO_3 nanoparticles possibly lead to microorganism cytotoxicity, which increases their bio-active impact and recommended them as an effective bactericidal compound.

Acknowledgements This paper is supported financially by the Academy of Scientific Research and Technology (ASRT), Egypt, under initiatives of Science Up Faculty of Science (Grant No. 6722).

Funding Open access funding provided by The Science, Technology & Innovation Funding Authority (STDF) in cooperation with The Egyptian Knowledge Bank (EKB).

Data Availability Statement This manuscript has associated data in a data repository. [Authors' comment: Authors are responsible for the correctness of the statements provided in the manuscript. The authors approved the version to be published].

Declarations

Conflict of interest The authors declare that they have no known competing financial interests or personal relationships that could have appeared to influence the work reported in this paper.

Open Access This article is licensed under a Creative Commons Attribution 4.0 International License, which permits use, sharing, adaptation, distribution and reproduction in any medium or format, as long as you give appropriate credit to the original author(s) and the source, provide a link to the Creative

Commons licence, and indicate if changes were made. The images or other third party material in this article are included in the article's Creative Commons licence, unless indicated otherwise in a credit line to the material. If material is not included in the article's Creative Commons licence and your intended use is not permitted by statutory regulation or exceeds the permitted use, you will need to obtain permission directly from the copyright holder. To view a copy of this licence, visit <http://creativecommons.org/licenses/by/4.0/>.

References

- S. Gul, M.A. Yousuf, A. Anwar, M.F. Warsi, P.O. Agboola, I. Shakir, M. Shahid, Al-substituted zinc spinel ferrite nanoparticles: preparation and evaluation of structural, electrical, magnetic and photocatalytic properties. *Ceram. Int.* **46**, 14195 (2020)
- N. Ghazi, H.M. Chenari, F.E. Ghodsi, Rietveld refinement, morphology analysis, optical and magnetic properties of magnesium-zinc ferrite nanofibers. *J. Magn. Magn. Mater.* **468**, 132 (2018)
- M.F. Warsi, A. Ifiikhar, M.A. Yousuf, M.I. Sarwar, S. Yousaf, S. Haider, M.F.A. Aboud, H. Shakir, S. Zulfiqar, Erbium substituted nickel-cobalt spinel ferrite nanoparticles: tailoring the structural, magnetic and electrical parameters. *Ceram. Int.* **46**, 24194 (2020)
- B. Pacakova, S. Kublckova, G. Salas, A.R. Mantikova, M. Marciello, M.P. Morales, D. Niznansky, J. Vejpravova, The internal structure of magnetic nanoparticles determines the magnetic response. *Nanoscale* **9**, 5129 (2017)
- M.A. Yousuf, M.M. Baig, N.F. Al-Khalli, M.A. Khan, M.F.A. Aboud, I. Shakir, M.F. Warsi, The impact of yttrium cations (Y^{3+}) on structural, spectral and dielectric properties of spinel manganese ferrite nanoparticles. *Ceram. Int.* **45**, 10936 (2019)
- A.M. Amanulla, S.K.J. Shahina, R. Sundaram, C.M. Magdalane, K. Kaviyarasu, D. Letsholathebe, S.B. Mohamed, J. Kennedy, M. Maaza, J. Photochem. Photobiol. B Biol. **183**, 233 (2018)
- S. Farhadi, J. Safabakhsh, P. Zaringhadan, Synthesis, characterization, and investigation of optical and magnetic properties of cobalt oxide (Co_3O_4) nanoparticles. *J. Nanostruct. Chem.* **3**, 69 (2013)
- M. Liong, J. Lu, M. Kovichich, T. Xia, S.G. Ruehm, A.E. Nel, F. Tamanoi, J.I. Zink, Multifunctional inorganic nanoparticles for imaging, targeting, and drug delivery. *ACS Nano* **2**, 889 (2008)
- Z.L. Wang, Zinc oxide nanostructures: growth, properties and applications. *J. Phys. Condens. Matter* **16**, 829 (2004)
- J.J. Vijaya, N. Jayaprakash, K. Kombaiah, K. Kaviyarasu, L.J. Kennedy, R.J. Ramalingam, H.A. Al-Lohedan, V.M.M. Ali, M. Maaza, J. Photochem. Photobiol. B Biol. **177**, 62 (2017)
- E. Ateia, L.M. Salah, A.A.H. El-Bassuony, Investigation of cation distribution and microstructure of nano ferrites prepared by different wet methods. *J. Inorg. Organomet. Polym.* **25**, 6 (2015)
- S.K. Jesudoss, J.J. Vijaya, L.J. Kennedy, P.I. Rajan, H.A. Al-Lohedan, R. Jathiramalingam, K. Kaviyarasu, M. Bououdina, Studies on the efficient dual performance of $Mn_{1-x}Ni_xFe_2O_4$ spinel nanoparticles in photodegradation and antibacterial activity. *J. Photochem. Photobiol. B Photobiol.* **165**, 121 (2016)
- E.E. Ateia, A.T. Mohamed, Core-shell nanoarchitectonics of $CoFe_2O_4$ encapsulated $La_2Fe_2O_6$ nanoparticles for their use in various applications. *J. Inorg. Organomet. Polym. Mater.* (2022). <https://doi.org/10.1007/s10904-021-02202-y>
- A. Mancuso, O. Sacco, V. Vaiano, D. Sannino, S. Pragliola, V. Venditto, N. Morante, Visible light active Fe-Pr co-doped TiO_2 for water pollutants degradation. *Catal. Today* **380**, 93–104 (2021)
- F. Raheem, M.A. Khan, A. Majeed, A. Hussain, M.F. Warsi, M.N. Akhtar, Structural, spectral, electrical, dielectric and magnetic properties of Yb doped Sr Ni Co-X hexagonal nano-structured ferrites. *J. Alloys Compd.* **708**, 903–910 (2017)
- A. Rahman, H. Sabeeh, S. Zulfiqar, P.O. Agboola, I. Shakir, M.F. Warsi, Structural, optical and photocatalytic studies of trimetallic oxides nanostructures prepared via wet chemical approach. *Synth. Met.* **259**, 116228 (2020)
- C.S. Vandana, B.H. Rudramadevi, *Mater. Res. Express* **5**, 046101 (2018)
- K. Kaviyarasu, P.P. Murmu, J. Kennedy, F.T. Thema, D. Letsholathebe, L. Kotsedi, M. Maaza, *Nucl. Instrum. Methods Phys. Res. Sect. B Beam Interact. Mater. At.* **409**, 147–152 (2017)
- A.A. Khan, A. Ahlawat, P. Deshmukh, D. Dileep, R. Singh, A.K. Karnal, S. Satapathy, *Ceram. Int.* **46**, 19682 (2020)
- A. Bashir, M. Ikram, R. Kumar, P.N. Lisboa-Filho, Structural, electronic structure and magnetic studies of $GdFe_{1-x}Ni_xO_3$ ($x \leq 0.5$). *J. Alloys Compd.* **521**, 183 (2012)
- A. Sultan, A. Mahmood, N.K. Goraya, A.M. Qureshi, I. Ahmad, M.N. Ashiq, I. Shakir, M.F. Warsi, *J. Alloys Compd.* **585**, 790 (2014)
- T. Kousar, I. Ahmad, M.A. Khan, G. Nasar, M. Shahid, I. Shakir, M.F. Warsi, *Ceram. Int.* **41**, 8578 (2014)
- S. Sahoo, P.K. Mahapatra, R.N.P. Choudhary, M.L. Nandagoswami, A. Kumar, Structural, electrical and magnetic characteristics of improper multiferroic: $GdFeO_3$. *Mater. Res. Express* **3**, 065017 (2016)
- L. Jiang, S. Yang, M. Zheng, H. Chen, A. Wu, *Mater. Res. Bull.* **104**, 92 (2018)
- P. Tirupathi, P. Justin, K. Prabahar, M. Poster, Broad temperature dependent magnetic and dielectric spectroscopy study of $Dy(Fe_{0.5}Cr_{0.5})O_3$ multiferroic ceramics. *J. Alloys Compd.* **731**, 411 (2018)
- W. Ma, H. Dong, *Thermal Barrier Coatings. A Volume in Woodhead Publishing Series in Metals and Surface Engineering*, (2011), p. 329
- E.E. Ateia, B. Hussein, C. Singh, N. Okasha, Study of physical properties of Co substituted $GdFeO_3$ orthoferrites and evaluation of their antibacterial activity. *J. Inorg. Organomet. Polym. Mater.* **30**, 4320–4328 (2020)
- A.M. Bolarin-Miro, F. Sanchez-De Jesus, C.A. Cortés-Escobedo, R. Valenzuela, S. Amnard, Structure and magnetic properties of $Gd_xY_{1-x}FeO_3$ obtained by mechano-synthesis. *J. Alloys Compd.* **586**, S90–S94 (2014)
- E.E. Ateia, M.K. Abdelmaksoud, H. Ismail, A study of the magnetic properties and the magneto-crystalline anisotropy for the nano-composites $CoFe_2O_4/Sm_{0.7}La_{0.3}FeO_3$. *J. Mater. Sci. Mater. Electron.* **32**, 4480–4492 (2021)
- A.W. Bauer, W.M. Kirby, C. Sherris, M. Turck, Antibiotic susceptibility testing by a standardized single disk method. *Am. J. Clin. Pathol.* **45**, 493 (1966)
- M.A. Pfaller, L. Burmeister, M.S. Bartlett, M.G. Rinaldi, Multicenter evaluation of four methods of yeast inoculum preparation. *J. Clin. Microbiol.* **26**, 1437 (1988)
- J.C. Chang, P.R. Hsueh, J.J. Wu, S.W. Ho, W.C. Hsieh, K.T. Luh, Antimicrobial susceptibility of flavobacteria as determined by agar dilution and disk diffusion methods. *Antimicrob. Agents Chemother.* **41**(6), 1301 (1997)
- W.J. Brown, National committee for clinical laboratory standards agar dilution susceptibility testing of anaerobic gram-negative bacteria. *Antimicrob. Agents Chemother.* **32**(3), 385–390 (1988)
- L.D. Liebowitz, H.R. Ashbee, E.G.V. Evans, Y. Chong, N. Mallatova, M. Zaidi, D. Gibbs, Global Antifungal Surveillance Group, *J. Diagn. Microbiol. Infect. Dis.* **4**, 27 (2001)
- M.J. Matar, L. Astrosky-Zeichner, V.L. Paetznick, J.R. Rodriguz, E. Chen, J.H. Rex, *J. Antimicrob. Agents Chemother.* **47**, 1647 (2003)

36. S. Shirasaki, K. Takahashi, K. Manabe, *Bull. Chem. Soc. Jpn.* **44**, 3189 (1971)
37. E.E. Ateia, A.T. Mohamed, Improvement of the magnetic properties of magnesium nanoferrites via $\text{CO}^{2+}/\text{Ca}^{2+}$ doping. *J. Supercond. Nov. Magn.* **30**, 627 (2017)
38. E.E. Ateia, A.T. Mohamed, M. Maged, A. Abdelazim, Crystal structures and magnetic properties of polyethylene glycol/polyacrylamide encapsulated $\text{CoCuFe}_4\text{O}_8$ ferrite nanoparticles. *Appl. Phys. A* **126**, 669 (2020)
39. K. Sultan, M. Ikram, K. Asakan, Structural, optical and dielectric study of Mn doped PrFeO_3 ceramics. *Vacuum* **99**, 251 (2014)
40. D. Xu, Y. Bu, W. Tan, Q. Zhong, Structure and redox properties of perovskite $\text{Y}_{0.9}\text{Sr}_{0.1}\text{Cr}_{1-x}\text{Fe}_x\text{O}_{3-\delta}$. *Appl. Surf. Sci.* **268**, 246 (2013)
41. S. Gupta, M.K. Mahapatra, P. Singh, Phase transformation, thermal expansion and electrical conductivity of lanthanum chromite. *Mater. Res. Bull.* **48**, 3262 (2013)
42. E.E. Ateia, H. Ismail, H. Elshimy, M.K. Abdelmaksoud, Structural and magnetic tuning of LaFeO_3 orthoferrite substituted different rare earth elements to optimize their technological applications. *J. Inorg. Organomet. Polym. Mater.* **31**, 1713–1725 (2021)
43. P. Kumar, R.K. Singh, A.S.K. Sinha, P. Singh, Effect of isovalent ion substitution on electrical and dielectric properties of LaCrO_3 . *J. Alloys Compd.* **576**, 154 (2013)
44. V.D. Nithya, R.J. Immanuel, S.T. Senthilkumar, C. Sanjeeviraja, I. Perelshtein, D. Zitoun, R.K. Selvan, Studies on the structural, electrical and magnetic properties of LaCrO_3 , $\text{LaCr}_{0.5}\text{Cu}_{0.5}\text{O}_3$ and $\text{LaCr}_{0.5}\text{Fe}_{0.5}\text{O}_3$ by sol–gel method. *Mater. Res. Bull.* **47**, 1861 (2012)
45. K.C. Verma, M. Singh, R.K. Kotnala, N. Goyal, Magnetic field control of polarization/capacitance/voltage/resistance through lattice strain in $\text{BaTiO}_3\text{-CoFe}_2\text{O}_4$ multiferroic nanocomposite. *J. Magn. Magn. Mater.* **469**, 483 (2019)
46. M.K. Mahata, K. Kumar, V.K. Rai, *Spectrochim. Acta A Mol. Biomol. Spectrosc.* **124**, 285 (2014)
47. A. Dahmani, M. Taïbi, M. Noguees, J. Aride, E. Loudghiri, A. Belayachi, Magnetic properties of the perovskite compounds $\text{YFe}_{1-x}\text{Cr}_x\text{O}_3$ ($0.5 \leq x \leq 1$). *Mater. Chem. Phys.* **77**, 912 (2003)
48. E. Brück, O. Tegus, D.T.C. Thanh, K.H.J. Buschow, Magnetocaloric refrigeration near room temperature. *J. Magn. Magn. Mater.* **310**, 2793 (2007)
49. I.R. Shein, K.I. Shein, V.L. Kozhevnikov, A.L. Ivanovskii, Band structure and the magnetic and elastic properties of SrFeO_3 and LaFeO_3 perovskites. *Phys. Solid State* **47**, 2082 (2005)
50. S. Husain, A.O.A. Keelani, W. Khan, Influence of Mn substitution on morphological, thermal and optical properties of nanocrystalline GdFeO_3 orthoferrite. *Nano-Struct. Nano-Objects* **15**, 17 (2018)
51. S.S.K. Ma, L. Chen, S. Zhang, J. Lin, S.P. Jiang, Syngas production by catalytic partial oxidation of methane over $(\text{La}_{0.7}\text{A}_{0.3})\text{BO}_3$ ($\text{A} = \text{Ba, Ca, Mg, Sr}$, and $\text{B} = \text{Cr or Fe}$) perovskite oxides for portable fuel cell applications. *Int. J. Hydrog. Energy* **38**, 13300 (2013)
52. J. Choi, B. Kim, S.H. Song, J.S. Park, *Int. J. Hydrog. Energy* **41**, 9619 (2016)
53. Y. Janbutrach, S. Hunpratub, E. Swatsitang, Ferromagnetism and optical properties of $\text{La}_{1-x}\text{Al}_x\text{FeO}_3$ nanopowders. *Nanoscale Res. Lett.* **9**, 498 (2014)
54. S. Thirumalairajan, K. Girija, V. Ganesh, D. Mangalaraj, C. Viswanathan, N. Ponpandian, Novel synthesis of LaFeO_3 nanostructure dendrites: a systematic investigation of growth mechanism, properties, and biosensing for highly selective determination of neurotransmitter compounds. *Cryst. Growth Des.* **13**, 291 (2013)
55. M.K. Sharma, K. Singh, K. Mukherjee, Exchange bias in a mixed metal oxide based magnetocaloric compound $\text{YFe}_{0.5}\text{Cr}_{0.5}\text{O}_3$. *J. Magn. Magn. Mater.* **414**, 116 (2016)
56. X. Zheng, Y. Li, W. You, G. Lei, Y. Cao, Y. Zhang, L. Jiang, Construction of Fe-doped TiO_{2-x} ultrathin nanosheets with rich oxygen vacancies for highly efficient oxidation of H_2S . *Chem. Eng. J.* **430**, 132917 (2022)
57. L. Capogna, A. Martinelli, M.G. Francesconi, P.G. Radaelli, J.R. Carvajal, O. Cabeza, M. Ferretti, C. Castellano, T. Corridoni, N. Pomero, Crystal and magnetic structures of $(\text{La}_{0.70}\text{Ca}_{0.30})(\text{Cr}_y\text{Mn}_{1-y})\text{O}_3$: a neutron powder diffraction study. *Phys. Rev. B* **77**, 104438 (2008)
58. H. Ahmadv, H. Salamati, P. Kameli, A. Poddar, M. Acet, K. Zakeri, Exchange bias in LaFeO_3 nanoparticles. *J. Phys. D Appl. Phys.* **43**, 245002 (2010)
59. R. Gupta, A.K. Pramanik, Site dilution in SrRuO_3 : effects on structural and magnetic properties. *J. Condens. Matter Phys.* **29**(11), 115801 (2017)
60. P. Shahi, R.K. Singh, R.K. Singh, S. Kumar, A. Tiwari, A. Tripathi, J. Saha, S. Patnaik, A.K. Ghosh, S. Chatterjee, Effect of dilution of both A- and B-sites on the multiferroic properties of spinal Mott insulators. *Mater. Res. Express* **2**, 076501 (2015)
61. G.A. Bain, J.F. Berry, Diamagnetic corrections and Pascal's constants. *J. Chem. Educ.* **85**, 532 (2008)
62. Z.L. Wang, Y. Liu, Z. Zhang, *Handbook of Nanophase and Nanostructured Materials: Materials Systems and Applications I*, vol. 3 (Kluwer Academic/Plenum Publishers, New York, 2003)
63. R.W. McCallum, Determination of the saturation magnetization, anisotropy field, mean field interaction, and switching field distribution for nanocrystalline hard magnets. *J. Magn. Magn. Mater.* **292**, 135–142 (2005)
64. R.K. Dwivedi, D. Kumar, O. Parkash, Valence compensated perovskite oxide system $\text{Ca}_{1-x}\text{La}_x\text{Ti}_{1-x}\text{Cr}_x\text{O}_3$ Part II Electrical transport behavior. *J. Mater. Sci.* **36**, 3649 (2001)
65. M.B. Mohamed, H. Wang, H. Fuess, Dielectric relaxation and magnetic properties of Cr doped GaFeO_3 . *J. Phys. D Appl. Phys.* **43**, 455409 (2010)
66. H. Khan, I.K. Swati, Fe^{3+} -doped anatase TiO_2 with d-d transition, oxygen vacancies and Ti^{3+} centers: synthesis, characterization, UV–vis photocatalytic and mechanistic studies. *Ind. Eng. Chem.* **55**, 6619 (2016)
67. J. Mizusaki, T. Sasamoto, W.R. Cannon, H.K. Bowen, Electronic conductivity, Seebeck coefficient, and defect structure of LaFeO_3 . *J. Am. Ceram. Soc.* **65**, 363 (1982)
68. M. Aghajanzadeh, E. Naderi, M. Zamani, A. Sharafi, M. Naseri, H. Danafar, In vivo and in vitro biocompatibility study of MnFe_2O_4 and $\text{Cr}_2\text{Fe}_6\text{O}_{12}$ as photosensitizer for photodynamic therapy and drug delivery of anti-cancer drugs. *Drug Dev. Ind. Pharm.* **46**, 846 (2020)
69. R. Meyer, R. Waser, Dynamic leakage current compensation in ferroelectric thin-film capacitor structures. *Appl. Phys. Lett.* **86**, 142907 (2005)
70. K. Kombaiyah, J.J. Vijaya, L.J. Kennedy, K. Kaviyarasu, R.J. Ramalingam, H.A. Al-Lohedan, Green synthesis of Co_3O_4 nanorods for highly efficient catalytic, photocatalytic, and antibacterial activities. *J. Nanosci. Nanotechnol.* **19**(5), 2590–2598 (2019)
71. Z. Shu, Y. Zhang, J. Ouyang, H. Yang, Characterization and synergetic antibacterial properties of ZnO and CeO_2 supported by halloysite. *Appl. Surf. Sci.* **420**, 833–838 (2017)
72. N. Kumar, A. Shukla, N. Kumar, S. Hajra, S. Sahoo, R.N.P. Choudhary, Structural, bulk permittivity and impedance spectra of electronic material: $\text{Bi}(\text{Fe}_{0.5}\text{La}_{0.5})\text{O}_3$. *J. Mater. Sci. Mater.* **30**, 1919 (2019)